Macromolecules
Cite This: Macromolecules 2019, 52, 7858−7869
Article
pubs.acs.org/Macromolecules

Spatial Demixing of Ring and Chain Polymers in Pressure-Driven Flow

Lisa B. Weiss,*,† Christos N. Likos,*,† and Arash Nikoubashman*,‡

†Faculty of Physics, University of Vienna, Boltzmanngasse 5, A-1090 Vienna, Austria
‡Institute of Physics, Johannes Gutenberg University Mainz, Staudingerweg 7, 55128 Mainz, Germany

Supporting Information

ABSTRACT: We investigate mixtures of ring and linear polymers in solution at various number ratios, ranging from pure chains to pure rings, and at densities around the overlap concentration. In bulk and at rest, we find a shrinking of both topologies with increasing polymer content of the solution. At the same time, we observe an increase in the solution viscosity with a concomitant reduction of the polymer diffusivity. When exposing ring-chain mixtures of any composition to a pressure-driven flow in a slit channel, we find that ring polymers always migrate toward the center, whereas chains populate the regions of high local shear close to the channel walls. Interestingly, in a pure chain solution, this cross-stream migration toward the walls is absent. This phenomenon could be used to iteratively separate chains and rings at high mass throughput in simple microfluidic devices using pressure-driven flows. Furthermore, we show how pressure-driven flow can be used as a computationally efficient approach for determining the shear viscosity of (complex) liquids.

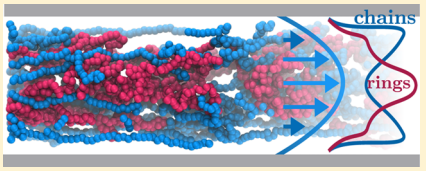

1. INTRODUCTION

In biology, the topology of polymers, as for example, a linear chain, a circular ring, or a knotted ring, is precisely controlled and has a direct impact on their properties, e.g., in the case of DNA[1−4] and RNA.[5,6] For instance, ring-shaped RNA is less prone to degradation compared to its linear counterpart.[5] Synthesis of polymers of precise topology can open new routes toward novel functional materials,[7] as for example, more biodegradable plastics.[8]

Besides being of interest in materials science, there is a fundamental interest in understanding the impact of topology on polymeric properties. In the case of ring and linear polymers, it has been shown that, in equilibrium and under dilute conditions, the size of ring and linear polymers increases in the same manner with the degree of polymerization.[9] In contrast, rings shrink more strongly than chains at concentrations above the overlap concentration.[10] Differences in dynamic properties become apparent for mixtures of chains and rings[11] and when such mixtures are entangled.[12−14] Moreover, when dilute solutions of rings are exposed to an elongational flow field, they show a unique coupling of the ring architecture to the flow field, leading to a reduced stretch in flow direction.[15,16] In the melt, ring polymers as pure as currently producible show a distinctly different response in rheological experiments compared to their linear analogue, lacking, for example, a rubber plateau.[17]

One major challenge in the synthesis of ring polymers is the production of batches with high topological purity, i.e., samples that contain solely (nonconcatenated) rings with narrow size distribution. This is owed to the fact that chemical approaches fail to distinguish macromolecules by topology, as they consist of exactly the same number and type of monomers. Due to the unique coupling of polymer architecture and flow fields,[15] microfluidic devices represent a promising route for topological sieving of molecules *after* the polymers have been synthesized. This strategy has the advantage that it can be seamlessly added to existing synthesis recipes and that it allows for a high throughput.

Microfluidic, nanofluidic, and lab-on-a-chip devices revolutionized the processing of soft matter with high precision. A high positional control of rigid particles dissolved in a Newtonian solvent has been first achieved by exploiting inertia.[18−20] When inertia is more important compared to viscous effects, characterized by a large Reynolds number *Re*, time reversibility of the Navier−Stokes equation is broken and the rigid particles can cross streamlines. In cylindrical channels, the particles form an annular distribution, due to the competition of lift forces form the parabolic flow profile, pushing the particles away from the channel center, and from the wall-induced asymmetry in the wake vorticity field, driving the particles away from the walls.[21,22] This strategy offers the advantage that focusing does not enforce the addition of any focusing agent and can be operated at high throughput. A drawback of this approach is that the number of focusing points depends strongly on the channel geometry and the latter must be tuned precisely to result in a proper 3D focusing.[19] Alternatively, 3D focusing of particles can also be achieved by adding an elastic agent, as for example, polymers, to the solution.[23,24] The so-called viscoelastic focusing operates typically in a regime where inertia is negligible, but when the

Received: August 3, 2019
Revised: September 19, 2019
Published: October 10, 2019

DOI: 10.1021/acs.macromol.9b01629
Macromolecules 2019, 52, 7858−7869

characteristic time of the added polymer exceeds the time scale associated with the flow, the Weissenberg number Wi exceeds unity. It was initially hypothesized that the condition of negligible inertia restricts the maximum flow velocity, at which such a device can be operated. However, recent experiments and simulations have shown that focusing can also be achieved at high flow strength when inertia becomes relevant again. In this case, the elastic and inertial forces are balanced, yielding, e.g., elastic-inertial particle focusing onto a single file in the center of a square channel.[25−27] Additionally, a regime where inertial effects dominate ($Re \gg 1$) in the presence of small elastic forces ($Wi < 1$) has been identified as an efficient focusing regime as well.[28] A detailed study in ref 29 highlights important regimes and underlying mechanisms of focusing, also examining the effect of shear thinning. When aiming at focusing deformable particles, such as cells and droplets, nonmonotonic behavior is reported in the viscoelastic[30,31] and elastic-inertial regime.[32]

We have recently proposed a microfluidic device with patterned channel walls for the high-purity filtering of chains and rings dispersed in Newtonian solvents at ultradilute conditions.[33] To enhance the mass throughput of polymers and to simplify the design of the microfluidic filter, we propose here an easy-to-build filtering device for purifying semidilute mixtures of ring and linear polymers. In our simulations, we find that ring polymers accumulate in the central region of the slit channel when exposed to a pressure-driven flow. In contrast, chains migrate only to the high shear region close to the walls, when rings are present in the solution. This phenomenon opens new routes toward the topological separation of chains and rings. We find that at concentrations below the overlap concentration, this effect is enhanced by hydrodynamic interactions (HI), but the effect itself persists as well at higher concentrations and in the absence of hydrodynamics. In Section 2, we discuss the employed simulation methods, followed in Section 3, by the bulk properties in equilibrium. Thereafter, we focus on the rheological properties of the polymer solutions in Section 4, before discussing the migration in microfluidic channels in detail in Section 5. The impact of hydrodynamics on migration and polymer conformations is discussed in Section 6.

2. MODEL AND SIMULATION DETAILS

We use a generic bead-spring model for the polymers, where each polymer consists of $M = 50$ spherical monomeric units with diameter a. The advantage of such a model lies in its transferability to polymers of distinct monomer chemistry, where a monomer represents a Kuhn segment. The inter- and intrapolymer excluded volume interaction between monomers is accounted for by the Weeks−Chandler−Andersen (WCA) potential,[34] describing a polymer dissolved in a good solvent[35]

$$U_{\mathrm{WCA}}(r_{ij}) = \begin{cases} 4\varepsilon\left[\left(\frac{a}{r_{ij}}\right)^{12} - \left(\frac{a}{r_{ij}}\right)^{6} + \frac{1}{4}\right] & \text{if } r_{ij} < 2^{1/6}a \\ 0 & \text{otherwise} \end{cases} \quad (1)$$

Here, r_{ij} denotes the distance between any two monomers i and j, and ε is the interaction strength. The total number of polymers in the solution, $N = N_{\mathrm{L}} + N_{\mathrm{R}}$, is composed of the number of linear polymers (chains) N_{L} and circular polymers (rings) N_{R}, each consisting of M monomers. Connectivity between monomers of a polymer is achieved through the finitely extensible nonlinear elastic (FENE) potential[36]

$$U_{\mathrm{FENE}} = \begin{cases} -\frac{k}{2}R_0^2 \ln\left(1 - \left(\frac{r_{i,i+1}}{R_0}\right)^2\right) & \text{if } r_{i,i+1} < R_0 \\ \infty & \text{otherwise} \end{cases} \quad (2)$$

In the case of linear polymers, the monomer index i runs from the first to the $(M-1)$th monomer, whereas for rings, it runs up to the Mth monomer, with $i + 1 \hat{=} 1$ when $i = M$ to ensure a closed loop. To avoid any unphysical bond crossing, we used the standard Kremer−Grest parameters,[37] $k = 30\varepsilon/a^2$ and $R_0 = 1.5a$. In this work, we consider bulk polymer solutions at rest and under shear, as well as solutions confined to a slit channel under pressure-driven flow. In the latter case, two planar walls confine the polymers in the z direction, as shown in Figure 1a.

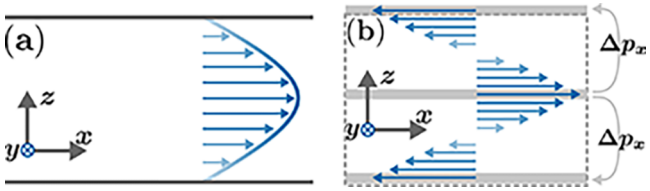

Figure 1. (a) Scheme of a slit channel, confined in gradient (z) direction with periodic boundary conditions in flow (x) and vorticity (y) directions. (b) Scheme of the reverse perturbation method with periodic boundary conditions in flow (x), vorticity (y), and gradient (z) directions. The highlighted gray layers represent the regions from which particles are selected for swapping events.

The walls are separated by a distance $2L_z$, which is on the same order of magnitude as the size of a polymer coil at rest. To model the purely repulsive wall potential, we use an integrated and shifted Lennard-Jones potential

$$U_{\mathrm{WM}} = \begin{cases} \varepsilon_{\mathrm{WM}}\left[\frac{2}{15}\left(\frac{a_{\mathrm{WM}}}{z_i}\right)^9 - \left(\frac{a_{\mathrm{WM}}}{z_i}\right)^3 + \frac{\sqrt{10}}{3}\right] & \text{if } z_i < \left(\frac{2}{5}\right)^{1/6} a_{\mathrm{WM}} \\ 0 & \text{otherwise} \end{cases} \quad (3)$$

Since the confinement is only acting in the z direction, the wall potential solely depends on the z coordinate of the monomers. Moreover, the parameters a_{WM} and $\varepsilon_{\mathrm{WM}}$ control the wall−monomer interaction length and its interaction strength, respectively, both of which have been set to unity.

To take into account HI, we employ the multiparticle collision (MPC) algorithm.[38−40] This approach enables us to bridge the characteristic time scale associated with a molecular solvent and the polymers. Hydrodynamics play an important role in many systems out of equilibrium and/or when complex boundaries are involved, as for example, in the case of polymer migration in microfluidic channels.[41−43] But even in dilute solutions at rest, HI have a significant impact on dynamic quantities, as for example, diffusivities, which can be described by Zimm dynamics.[40,44,45] With increasing monomer concentration, HI are screened and dynamics in a linear polymer melt can be described by the Rouse model.[35,46]

The MPC algorithm is based on stochastically interacting point particles, which undergo consecutive streaming and collision steps. During the streaming step, the particles are propagated ballistically

DOI: 10.1021/acs.macromol.9b01629
Macromolecules 2019, 52, 7858−7869

$$\mathbf{r}_i(t + \Delta t_C) = \mathbf{r}_i(t) + \mathbf{v}_i(t)\Delta t_C \tag{4}$$

where $\mathbf{r}_i$ is the position of solvent particle i and $\mathbf{v}_i$ is its velocity. In the collision step, first, a three-dimensional grid of cell length $a_S = a$ is overlaid on the simulation box. Then, the center of mass velocity $\mathbf{v}_{CoM}$ is calculated within each cell. Subsequently, the relative velocity of each particle in the cell is rotated around a randomly oriented axis by a fixed angle α, described by the operator $\mathbf{\Omega}_\alpha$

$$\mathbf{v}_i(t + \Delta t_C) = \mathbf{v}_{CoM}(t) + \Omega_\alpha(\mathbf{v}_i(t) - \mathbf{v}_{CoM}(t)) \tag{5}$$

Since this procedure conserves the local energy, momentum, and mass, the Navier−Stokes equation is fulfilled and HI are reproduced down to the size of a collision cell.[47] Note that the introduction of collision cells violates Galilean invariance, when the mean free path of the particles between collisions is smaller than the cell size. To restore Galilean invariance, a random grid shift in the interval of $[-a_S/2, a_S/2]$ is performed before each collision step in all spatial directions.[48,49] Commonly, the thermal energy k_BT, the mass of a solvent particle m_S, and the length of a collision cell a_S are set to unity, defining the units of time $t_0 = \sqrt{m_S/(k_BT)}\, a_S$. In this work, we employ an average number density of solvent particles of $\rho_S = 5a_S^{-3}$, a collision time step of $\Delta t_C = 0.1t_0$, and a rotation angle of $\alpha = 130°$, resulting in an analytically calculated dynamic viscosity $\eta = 3.96\, m_S/(a_S t_0)$ and a kinematic viscosity of $\nu = \eta/\rho_S = 0.79 a_S^2/t_0$.[50,51] This set of parameters reproduces a liquidlike behavior of the coarse-grained solvent.[52] To simulate a buoyant monomer, we set the monomer mass m_M equal to the average mass of a collision cell filled with solvent particles only, thus $m_M = \rho_S m_S a_S^3 = 5m_S$. Pressure-driven flow is achieved by applying a body force $f_x = m_S g_x$ to all solvent particles in combination with stick boundary conditions at the channel walls, which quickly saturates to a steady-state flow profile. To model stick boundary conditions between the solvent and the wall, we employ bounce-back rules in combination with virtual particles.[53,54] Applying a body force is equivalent to a pressure-driven flow in a channel of constant cross section. The pure MPC solvent behaves as a Newtonian fluid and a parabolic flow profile develops

$$u_x(z) = \frac{u_{max}}{L_z^2}(L_z^2 - z^2) \tag{6}$$

where $u_{max} = f_x \rho_S L_z^2/2\eta$ is the maximum flow velocity in the channel center $z = 0$ and L_z is half the channel width.

The temperature is kept constant at $k_BT = 1$ by employing a cell-level Maxwellian thermostat.[55] The coupling of the solvent to the monomers is achieved through participation of the latter in the collision step. During the solvent streaming step, 25 MD steps with time step $\Delta t_{MD} = 0.004t_0$ are performed. Bulk simulations are performed in a cubic box with $L_x = L_y = L_z = L = 30a_S$, whereas the slit channel has a dimension of $L_x = 75a_S$, $L_y = 2L_z = 25a_S$, as depicted in Figure 1a.

Shear flow in the bulk solutions is achieved through the reverse perturbation method,[56−58] as shown in Figure 1b. Here, a shear stress σ_{xz} is imposed on the MPC solvent, by first dividing the simulation box into layers of thickness a along the gradient direction (z) and then swapping the velocities of particle i in the layer $a = 0$ with the largest negative x-velocity and particle j in the layer $a = L/2$ with the largest positive velocity in the x direction. By varying the frequency of swapping events as well as the number of particles partaking in it, the momentum flux $\langle \Delta p_x \rangle$ can be controlled. The shear stress σ_{xz} can then be computed through

$$\sigma_{xz} = \frac{\langle \Delta p_x \rangle}{2\Delta t L^2} \tag{7}$$

Here, Δt is the time interval after which a swapping event occurs and L is the length of the cubic simulation box. The shear rate $\dot{\gamma}$ can be extracted from the steady-state flow profile.

To elucidate the effect of HI, we have performed additional Langevin dynamics simulations, in which HI are absent. Here, the motion of a single monomer i is governed by

$$m_M \ddot{\mathbf{r}}_i = \mathbf{F}(\mathbf{r}_i) - \zeta(\dot{\mathbf{r}}_i - \mathbf{v}_S(\mathbf{r}_i)) + \sqrt{2\zeta k_B T}\,\mathbf{R}_i(t) \tag{8}$$

Here, $\dot{\mathbf{r}}_i$ represents the time derivative of the position vector $\mathbf{r}_i$, $\mathbf{F}_i$ is the conservative force acting on particle i due to the potentials defined in eqs 1, 2, and 3, $\mathbf{v}_S(\mathbf{r})$ is the imposed solvent velocity profile at position $\mathbf{r}$, which is set to zero in equilibrium, ζ is the friction coefficient, and R_i^α is an uncorrelated random Gaussian process for each particle i and Cartesian component $\alpha \in [x, y, z]$ with zero mean and variance one, as indicated below

$$\langle R_i^\alpha(t) \rangle = 0 \tag{9}$$

$$\langle R_i^\alpha(t) R_j^\beta(t') \rangle = \delta_{ij}\delta_{\alpha\beta}\delta(t - t') \tag{10}$$

Due to the lack of HI, the diffusive motion of the polymer center of mass is determined as

$$D = \frac{k_B T}{\zeta M} \tag{11}$$

following Rouse dynamics. We have verified that our Langevin simulations reproduce this theoretical description.

We characterized the conformation of the polymers by the components of the gyration tensor $\hat{\mathbf{G}}$

$$\hat{G}_{\alpha,\beta} = \frac{1}{M}\sum_{i=1}^{M} s_{i,\alpha} s_{i,\beta} \tag{12}$$

where α and β are the Cartesian components $\in [x, y, z]$ and $\mathbf{s}_i$ is the position of monomer i in the center of mass reference frame of the corresponding polymer. The hat indicates instantaneous values, whereas in the absence of the hat, we refer to time-averaged quantities. The radius of gyration $\hat{R}_g$ can be calculated *via* the trace of the gyration tensor $\hat{\mathbf{G}}$

$$\hat{R}_g = \sqrt{\mathrm{tr}(\hat{G})} \tag{13}$$

We focus in this work on linear and ring polymer solutions around the overlap concentration c^*, which is defined as the concentration at which the total volume V is pervaded by polymers[35]

$$\frac{V_P}{V} = \frac{4\pi R_g^3 N}{3V} = \frac{4\pi R_g^3}{3} c^* = 1 \tag{14}$$

Equation 14 defines the overlap concentration c^* for pure chains or pure rings employing their radius of gyration at infinite dilution. In mixtures of chains and rings, the concentration of rings at c^* for any ratio of N_L:N_R is defined as follows

DOI: 10.1021/acs.macromol.9b01629
Macromolecules 2019, 52, 7858−7869

$$\frac{4\pi}{3}\left(R_{g,R}^3\frac{N_R}{V}+R_{g,L}^3\frac{N_L}{V}\right)$$
$$=\frac{4\pi}{3}(R_{g,R}^3+R_{g,L}^3)\left(1+\frac{N_L}{N_R}\right)\frac{N_R}{V}$$
$$=1 \quad (15)$$

By defining the ratio N_L:N_R, the number of rings at the overlap concentration can be calculated according to eq 15. By multiplying the ring concentration by the ratio N_L:N_R, one obtains the chain concentration.

We characterize the flow through the dimensionless Reynolds number Re and Weissenberg number Wi

$$Re=\frac{2uL_z}{\nu} \quad (16)$$

$$Wi=\tau\dot{\gamma} \quad (17)$$

In eq 16, u is the characteristic flow velocity, which we approximate by u_{max}, $2L_z$ is the channel width, and ν is the kinematic viscosity. In eq 17, τ is the polymers' longest relaxation time and $\dot{\gamma}$ is the characteristic shear rate, approximated by $\dot{\gamma}\approx u_{max}/L_z$. Note that the kinematic viscosity ν depends on the concentration c, the composition N_L:N_R, as well as the shear rate, since the polymer solutions are shear thinning. To characterize the elasticity of the solution, we introduce the elasticity number El

$$El=\frac{Wi}{Re} \quad (18)$$

3. EQUILIBRIUM PROPERTIES IN BULK

We have studied mixtures of chain and ring polymers at various number ratios N_L:N_R and multiples of the overlap concentration c^*. Table 1 summarizes the equilibrium properties of chain and ring polymers at infinite dilution and in the presence of HI, such as the radius of gyration $R_{g,c\to0}$, the diffusion coefficient $D_{c\to0}$, and the relaxation time $\tau_{c\to0}$. Here, we have calculated the relaxation time as the time a polymer takes to diffuse over its diameter $2R_g$.

Table 1. Equilibrium Properties of Single Linear and Circular Polymers of M = 50 Monomers at Infinite Dilution and in the Presence of HI[a]

	$R_{g,c\to0}$ [a_S]	$D_{c\to0}$ [$a_S^2t_0^{-1}$]	$\tau_{c\to0}$ [t_0]
linear	4.804 ± 0.003	(4.8 ± 0.7) × 10^{-3}	3200 ± 500
ring	3.560 ± 0.002	(5.1 ± 0.9) × 10^{-3}	1700 ± 300

[a] $R_{g,c\to0}$ denotes the radius of gyration, $D_{c\to0}$ is the diffusion coefficient corrected for finite size effects,[59] and $\tau_{c\to0}$ is the longest relaxation time determined as the time a polymer takes to diffuse over its diameter $2R_g$. The box length is $L=30a_0$.

Due to the topological restriction, rings are smaller than chains. However, rings and chains exhibit the same scaling behavior with M regarding their overall sizes. For example, the radius of gyration scales as $R_g\propto(M-1)^{\nu_F}$, with Flory exponent $\nu_F=3/5$ for polymers dissolved in a good solvent at dilute conditions. The hydrodynamic radius of ring polymers is smaller as well, thus increasing their diffusivity compared to their linear counterpart according to the Stokes−Einstein law in the presence of hydrodynamics. The R_g values indicated in Table 1 are used to calculate the number concentration of chain polymers and ring polymers at the overlap concentration c^*. As $R_{g,c\to0}$ for chains is larger compared to rings, the number of chains at c^* is lower than for rings according to eq 14 in a pure solution. When looking at mixtures of chains and rings, we define the ratio of chains to rings via the number ratio of chains N_L to rings N_R, as given in eq 15. Hence, for a number ratio N_L:N_R = 1:1, a larger volume is occupied by chains than by rings. Table 2 summarizes N_L and N_R for all compositions and concentrations employed. Additionally, the polymer concentration c_P and monomer concentration $c_M=(NM)/V$, with N the total number of polymers and M the number of monomers per polymer, as well as the monomer volume fraction $\phi_M=\pi c_M a_S^3/6$ are indicated. We can deduce from this table that the polymer concentration and thus the monomer concentration increase strongly with increasing fraction of ring polymers for a fixed multiple of the overlap concentration.

Figure 2a shows the radius of gyration as a function of the concentration in a log−log plot. With increasing concentration c, both polymer types shrink due to steric crowding. Consistent with previous results,[60] shrinking sets in already below $c=c^*$. Scaling theory predicts that R_g of linear chains will shrink according to

$$R_g\approx R_{g,c\to0}\left(\frac{c}{c^*}\right)^{-(\nu_F-1/2)/(3\nu_F-1)} \quad (19)$$

for concentrations larger than the overlap concentration,[35] as shown experimentally[61] and computationally.[60] Since this scaling is only recovered well above the overlap concentration c^* and for sufficiently long chains (see Figure 1 in ref 60), we do not cover this regime in our work, which is limited to [0.5 − 2.0] c^* for a fixed chain length of M = 50. It has been shown that rings shrink in the semidilute regime with

$$R_g\approx R_{g,c\to0}\left(\frac{c}{c^*}\right)^{-(\nu_F-\omega)/(3\nu_F-1)} \quad (20)$$

with $\omega=2/5$ for rings of a contour length shorter than the entanglement length and $\omega=1/3$ for very long, entangled ring polymers.[10,62] Employing $\omega=2/5$ results in an overall exponent of $-\frac{\nu_F-2/5}{3\nu_F-1}\approx-1/4$, whereas for chains it is $\frac{\nu-1/2}{3\nu-1}\approx-1/8$.[10] Qualitatively, we see in the limited data range available here that rings shrink more strongly compared to chains with increasing concentration c. However, we have not yet reached the theoretically predicted scaling behavior, due to the relatively short chain length (M = 50). The inset in Figure 2a shows the normalized radius of gyration as a function of the monomer concentration c_M in a log−log representation. Due to the short chain length in combination with the excluded volume interaction between monomers, we observe a decrease of R_g with monomer concentration. For a fixed multiple of the overlap concentration, the monomer concentration decreases with increasing degree of polymerization M. Thus, the observed dependence on c_M is stemming from the short chain length. Figure 2b shows the diffusivity of circular and linear polymers as a function of the monomer concentration c_M as well as the monomer volume fraction ϕ_M. As the monomer concentration increases, the diffusivity decreases, as expected from the concomitant increase in viscosity (see Section 4). The employed polymer length results in relatively high monomer volume fractions ϕ_M and monomer concentrations c_M showing a strong impact on diffusion.[63]

DOI: 10.1021/acs.macromol.9b01629
Macromolecules 2019, 52, 7858−7869

Table 2. Number of Chains N_L and Rings N_R for all Composition Ratios at Various Multiples of the Overlap Concentration c^* in a Cubic Box of $L = 30a_S$[a]

N_L:N_R	c	N_L	N_R	c_P $[a_S^{-3}]$	c_M $[a_S^{-3}]$	ϕ_M	K	n	$\nu_{eff}(\dot{\gamma}_1)$	$\nu_{eff}(\dot{\gamma}_2)$
chains	0.5c^*	28	0	0.0010	0.05	0.03	3.4(0)	0.88(8)	1.00	0.92
	1.0c^*	56	0	0.0021	0.10	0.05	3.8(6)	0.88(0)	1.20	1.09
	2.0c^*	112	0	0.0041	0.21	0.11	4.4(2)	0.83(8)	1.64	1.44
3:1	0.5c^*	27	9	0.0013	0.07	0.04	3.4(6)	0.88(1)	1.05	0.96
	1.0c^*	54	18	0.0027	0.13	0.07	4.0(1)	0.86(9)	1.29	1.16
	2.0c^*	108	36	0.0053	0.27	0.14	4.6(3)	0.82(0)	1.87	1.61
1:1	0.5c^*	21	21	0.0016	0.08	0.04	3.5(5)	0.87(8)	1.09	1.00
	1.0c^*	42	42	0.0031	0.16	0.08	4.1(5)	0.86(1)	1.38	1.24
	2.0c^*	84	84	0.0062	0.31	0.16	4.8(2)	0.80(2)	2.15	1.81
1:3	0.5c^*	13	39	0.0019	0.10	0.05	3.6(9)	0.87(2)	1.16	1.05
	1.0c^*	26	78	0.0039	0.19	0.10	4.2(6)	0.87(2)	1.16	1.05
	2.0c^*	52	136	0.0077	0.39	0.20	4.9(9)	0.76(5)	2.72	2.20
rings	0.5c^*	0	72	0.0027	0.13	0.07	3.9(2)	0.86(4)	1.28	1.15
	1.0c^*	0	144	0.0053	0.27	0.14	4.4(6)	0.81(4)	1.84	1.58
	2.0c^*	0	288	0.0106	0.53	0.28	5.0(8)	0.72(7)	4.13	3.17

[a]The overall concentration of polymers c_P and monomers c_M is indicated, as well as the volume fraction of monomers ϕ_M. Flow consistency index, K, and flow behavior index, n, form fits to a power-law fluid model (see Section 4 for details). Values in parentheses indicate measurement uncertainty in the last significant digit. Kinematic viscosity ν_{eff} in units of a_S/t_0^2 at two effective shear rates $\dot{\gamma}_1 < \dot{\gamma}_2$ approximated by u_{max}/L_z.

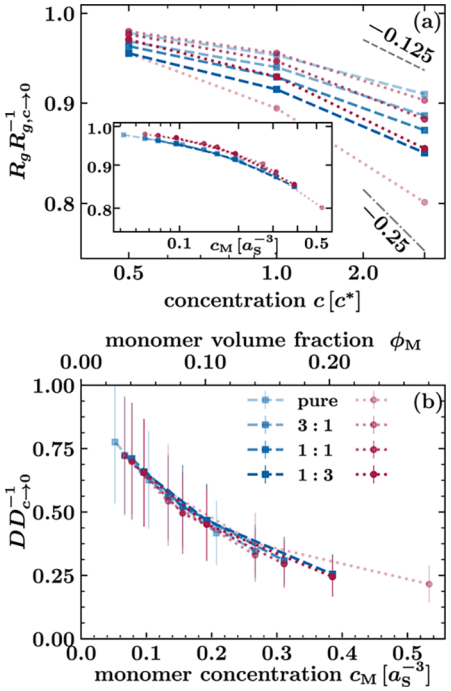

Figure 2. (a) Radius of gyration R_g normalized by the one in infinite dilution as a function of the concentration scaled over its overlap value c^* in a log−log plot. The gray dashed line indicates the prediction of eq 19 with exponent −1/8, and the gray dashed dotted line indicates the prediction of eq 20 with $\omega = 2/5$ resulting in an exponent of −1/4. The inset shows the same quantity as a function of the monomer concentration c_M in a log−log plot. (b) Normalized diffusion coefficient D as a function of the monomer concentration c_M and the monomer volume fraction ϕ_M. Results for chains and rings are shown as blue squares and red circles, respectively. The number ratios are indicated as N_L:N_R. Distinct hues correspond to distinct compositions N_L:N_R. The legend in (b) applies to (a) as well.

Experimentally, it has been shown that linear and ring polymer mixtures above the entanglement concentration show an impact of topology on diffusion.[13,14] Given the fact that we consider polymers of $M = 50$, we conclude that we are below the entanglement regime.

4. RHEOLOGICAL PROPERTIES

In this section, we determine the shear viscosity of the polymer solutions by applying a flow and measuring the resulting nonequilibrium response. In the case of a Newtonian fluid, the viscosity η is the proportionality constant between the shear rate $\dot{\gamma}$ and the shear stress σ_{xz}. For a non-Newtonian fluid, this linear relation does not hold anymore. However, one can introduce an effective viscosity $\eta_{eff}(\dot{\gamma})$, which is a function of the shear rate itself. For a power-law fluid, the relationship between σ_{xz} and $\dot{\gamma}$ is given by

$$\sigma_{xz} = K\dot{\gamma}^n = K\dot{\gamma}^{n-1}\dot{\gamma} = \eta_{eff}(\dot{\gamma})\dot{\gamma} \tag{21}$$

where n is the flow behavior index and K is the flow consistency index. In the case of $n = 1$, a Newtonian fluid is recovered and $K = \eta$. For $n < 1$, the solution is shear thinning, whereas it is shear thickening for $n > 1$.

In the first approach, we confine the solutions in a slit channel, apply a body force, and measure the resulting solvent flow profile, as shown in Figure 3. With increasing monomer concentration, the flow is more slowed down, indicating an increase in viscosity. Furthermore, we can identify a distinct flattening of the velocity profiles which is indicative of the shear thinning caused by the presence of polymers. The impact of polymers on the flow profile can be described by the solvent velocity for a power-law fluid

$$u_x(z) = \frac{n}{n+1}\left(\frac{f_x \rho_S L_z^{n+1}}{K}\right)^{1/n}\left(1 - \left(\frac{|z|}{L_z}\right)^{(n+1)/n}\right) + u_W \tag{22}$$

In eq 22, $u_x(z)$ is the solvent velocity, u_W is the slip velocity at the walls (zero for stick boundary conditions), f_x is the body force applied to solvent particles only, L_z is half of the channel width, and ρ_S is the number density of solvent particles. Furthermore, n and K describe the same parameters as in eq 21. Two distinct body forces $f_1 = 0.0045 m_S a_S t_0^{-2}$ and $f_2 = 2f_1$

DOI: 10.1021/acs.macromol.9b01629
Macromolecules 2019, 52, 7858−7869

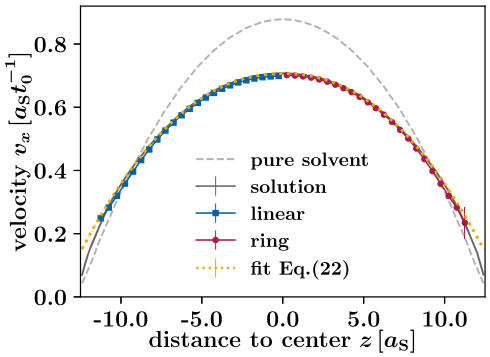

Figure 3. Velocity profile of the MPC solvent for the pure solvent in gray dashed lines, for a composition of N_L:N_R = 1:1 and $c = c^*$ in gray solid lines. The center of mass velocity of chains (rings) is shown in blue (red), for only half of the velocity profile. Additionally, a power-law fluid fit according to eq 22 is shown in yellow determining the fitting parameters n and K. These parameters lead to the effective kinematic viscosity $\nu_{eff} = 1.24 a_S^2/t_0$ of the solution (see main text) resulting in a Reynolds number of $Re = 14.2$ and a Weissenberg number $Wi = 303$ ($Wi = 158$) and an elastic number of $El = 21$ ($El = 11$) for chains (rings).

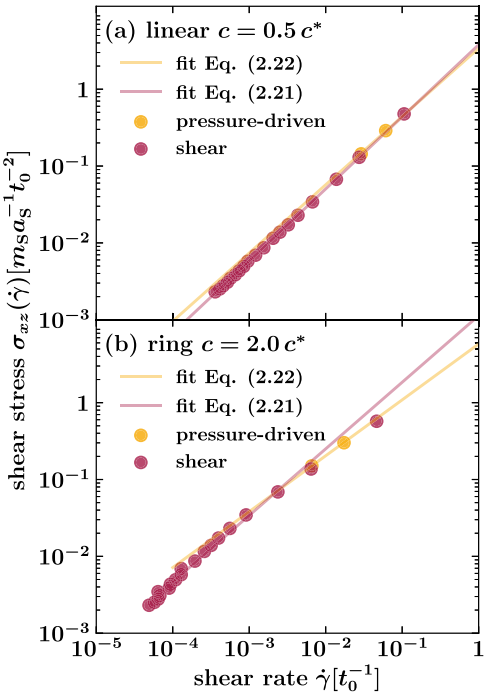

Figure 4. Shear stress σ_{xz} as a function of shear rate $\dot\gamma$ for a pure solution (a) of chains at $c = 0.5c^*$ and (b) of rings at $c = 2c^*$. Red refers to shear simulations, and yellow to pressure-driven flow simulations. The dots indicate measured data, while the lines represent fits according to eqs 21 and 22. Fitting parameters are indicated in Table 2 for pressure-driven flows, for shear simulations in (a) $K = 3.8 \pm 0.1$ and $n = 0.94 \pm 0.003$ and in (b) $K = 13.5 \pm 2.6$ and $n = 0.87 \pm 0.02$.

are employed for each set of concentration and composition. We fit the solvent flow profiles, as exemplarily depicted for a composition of N_L:N_R = 1:1 and $c = c^*$ in Figure 3, via eq 22 using n, K, and u_W as fit parameters and restricting the fit to $[-L_z + R_g; L_z - R_g]$. The average of the fitted parameters n and K for each set of concentration and composition is subsequently employed to derive an effective shear viscosity and shear stress via eq 21 using the effective shear rate $\dot\gamma_{eff} = u_{max}/L_z$. Dividing the effective shear viscosity, η_{eff}, by the solution's density results in the effective kinematic viscosity ν_{eff}. Here, we take error propagation explicitly into account emphasizing the consistency of the fits for the two flow strengths by the small error. The fitting parameters n and K as well as ν_{eff} for the two employed body forces are summarized in Table 2 and coincide well with literature values.[64,65] Applying the same body force to distinct systems does not yield the same effective shear rate $\dot\gamma$, as u_{max} varies with concentration and composition, as well as flow rate.

To verify the reliability of this approach, we performed additional shear simulations for pure solutions of rings and chains at $c = 0.5c^*$, c^* and $2c^*$ determining n and K via eq 21. These results are shown in Figure 4a for chains at $c = 0.5c^*$ and in Figure 4b for rings at $c = 2.0c^*$. Shear data are shown in red, where each dot corresponds to a simulation at a specific shear rate. The fit obtained by eq 21 is shown as a red line. Moreover, we employ the fitted parameters in pressure-driven flow, as indicated in Table 2 and predict the shear stress σ_{xz} via eq 21, shown as a yellow line. To illustrate the employed flow strengths in pressure-driven flows, the effective shear rate $\dot\gamma_{eff} = u_{max}/L_z$ and the corresponding shear stress σ_{xz} are shown in Figure 4 as yellow dots calculated via eq 21.

There is an excellent agreement between shear and pressure-driven flows for all investigated concentrations, exemplary shown in Figure 4a for a pure solution of chains at $c = 0.5c^*$. Only for ring polymers at $c = 2c^*$, as depicted in Figure 4b, we observe a deviation caused by the effect that eq 21 does not seem to accurately describe the shear data over the whole regime of shear rates probed. Note that even in this case, the results from pressure-driven flow agree well with those from the shear simulations at high shear rates. It is evident that we can recover with a single simulation of pressure-driven flow, multiple shear simulations, due to the nonlinear spatial variation of the flow field. Furthermore, simulations of pressure-driven flow at two different flow strengths result in consistent predictions. This result in itself is very promising as it allows to reduce the computational time for determining the flow properties of complex liquids. In general, we assume that three prerequisites are of importance for achieving accurate measurements: (i) a channel width, which is at least two times larger than the particle diameter so that the confinement effects are negligible; (ii) fitting the flow profile in regions accessible to the solute, i.e., excluding the regions where the solute is depleted; and (iii) a cross-stream diffusion of the polymer that is slower than its relaxation so that the particles have sufficient time to reach their steady-state conformation.

5. CROSS-STREAM MIGRATION IN NANOCHANNELS

When exposed to pressure-driven flows in nanochannels, mixtures of chain and ring polymers show a surprising cross-stream migration. We investigate the relative concentration of chains and rings along the gradient direction, $c_r(z)$, at rest and when exposed to pressure-driven flow. We define $c_r(z)$ as the local concentration $c(z)$, normalized by the average concentration c_0. To facilitate the comparison of chains and rings, we show chain properties for $z < 0$ and ring properties for $z > 0$. Evidently, for all systems but the pure ones, the ring and chain distributions are present in both parts of the channel. Figure 5a,b shows $c_r(z)$ for a solution in equilibrium at (a) $c = 0.5c^*$ and (b) $c = 2c^*$. Since the setup is mirror-symmetric with respect to the midplane, only half of the profile is shown. Due

DOI: 10.1021/acs.macromol.9b01629
Macromolecules 2019, 52, 7858−7869

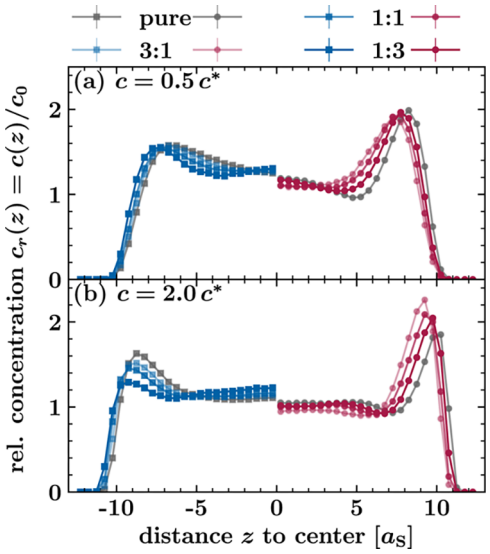

Figure 5. Relative concentration of chains and rings at rest versus distance to the channel center, z, for (a) $c = 0.5c^*$ and (b) $c = 2c^*$, at various number ratios of N_L:N_R. Due to the symmetry of the setup, only half of the concentration profile is depicted; chains' profile is shown for $z < 0$, rings' profile for $z > 0$. The pure systems, either only chains or only rings, are shown in gray. Red color corresponds to rings in topological mixtures, and blue color corresponds to chains. Monomer concentration and ring polymer content increase with darkening color.

to steric hindrance, chains and rings are depleted in the proximity ($\approx R_g$) of the walls. Chains and rings start to accumulate after this depletion zone, a phenomenon which is much more pronounced for rings compared to chains, congruent with results from density functional theory.[66] Since ring polymers consist of the same number of monomers, but have a smaller radius of gyration compared to chains, the effective monomer density is higher and they are in this sense "harder" and more colloid-like. This peak moves closer to the walls for both chains and rings with increasing monomer concentration, which can be realized by either an increase of concentration in units of c^* or an increase of ring polymer fraction at a fixed concentration in units of c^*.

Next, we investigate the impact of flow on the relative concentrations within a channel. To do so, we have chosen two flow strengths, which we characterize by the Reynolds number *Re*, Weissenberg number *Wi* and elastic number *El*, as defined in eqs 16−18. When calculating *Wi* for chains and rings, we explicitly take into account the increase of relaxation time with increasing concentration. Since we find that *Wi* of rings is approximately half of the one for chains, we indicate in Figure 6 only *Wi* and *El* of the chains. The kinematic viscosity ν employed in the calculation of the Reynolds number *Re* is derived from the effective shear viscosity, as defined in eq 21, where n and K were obtained by a power-law fit to the solvent flow profile, as noted in eq 22 and summarized in Table 2 (compare Section 4). The hydrodynamic numbers *Re*, *Wi*, and *El* depend strongly on concentration and flow strength, but weakly on composition. Thus, we characterize the flow strengths employed in Figure 6 using composition-averaged hydrodynamic numbers. Figure 6a−d shows how the relative densities of chains and rings are affected by flow. Figure 6a,c shows the relative densities for $c = 0.5c^*$ for a body force of $f_1 = 0.0045 m_S a_S t_0^{-2}$ and $f_2 = 2f_1$, respectively. Figure 6b,d shows the same quantities for $c = 2c^*$. Independent of concentration and flow strength, rings accumulate in the channel center, whereas chains have a higher probability to be close to the channel walls only in chain-ring mixtures. In a pure solution of chains (shown in gray for $z < 0$), linear polymers migrate toward the channel center as well.

How the local ratio $\chi(z)$ between number of chains and number of rings changes with the distance z from the channel center is shown in Figure 7 for $c = 2c^*$. First of all, for all average compositions N_L:N_R = 3:1 (Figure 7a), N_L:N_R = 1:1 (Figure 7b), and N_L:N_R = 1:3 (Figure 7c), the average ratio, shown as a gray dotted line, is never recovered, even when the solution is at rest, shown in yellow. Congruent with Figure 5, at rest, rings accumulate close to the walls and form layers. Thus, they deplete in the channel center in equilibrium. At the same time, chains show less tendency to accumulate close to the

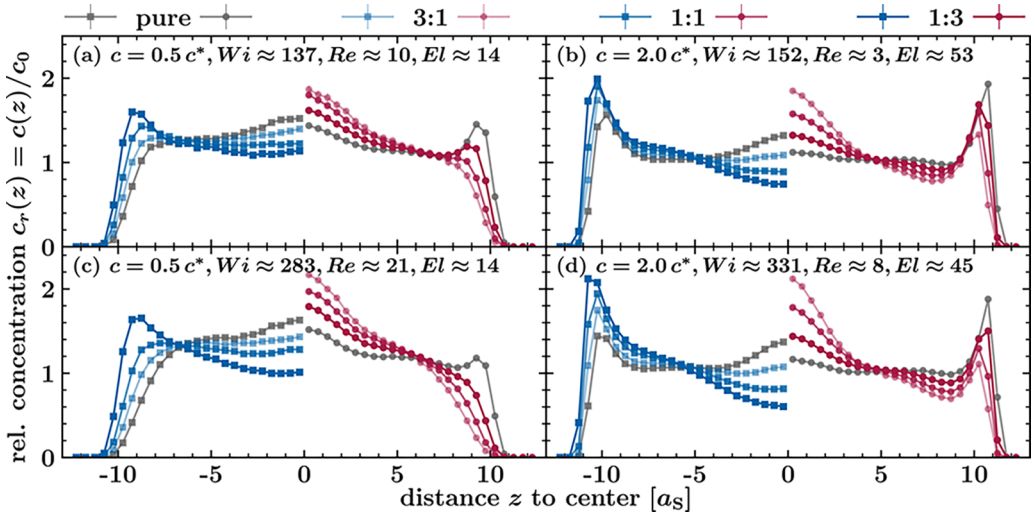

Figure 6. Relative concentration of polymers chains and rings in pressure-driven flow. (a, c) Systems at $c = 0.5c^*$; flow strength increases from (a) to (c). (b, d) Systems at $c = 2c^*$; flow strength increases from (b) to (d). The number ratios are indicated as N_L:N_R. Chains' profile is shown for $z < 0$, and rings' profile is shown for $z > 0$. Pure chain and ring systems are shown in gray. Red color corresponds to rings in topological mixtures, and blue color corresponds to chains. The monomer concentration and ring content increase with darkening color.

DOI: 10.1021/acs.macromol.9b01629
Macromolecules 2019, 52, 7858−7869

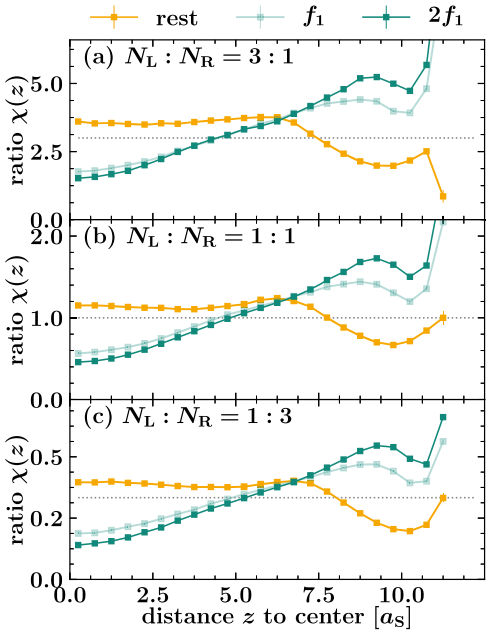

Figure 7. Number ratio χ of chains compared to rings as a function of the distance to the channel center at $c = 2c^*$ for an average composition of (a) N_L:N_R = 3:1, (b) N_L:N_R = 1:1, and (c) N_L:N_R = 1:3. The yellow lines show the local ratio in equilibrium, while the green lines correspond to pressure-driven flows with f_1 = 0.0045 $m_S a_S t_0^{-2}$ and f_2 = 2 f_1 = 0.009 $m_S a_S t_0^{-2}$; the darker the color, the stronger the flow. The gray dotted line indicates the average composition.

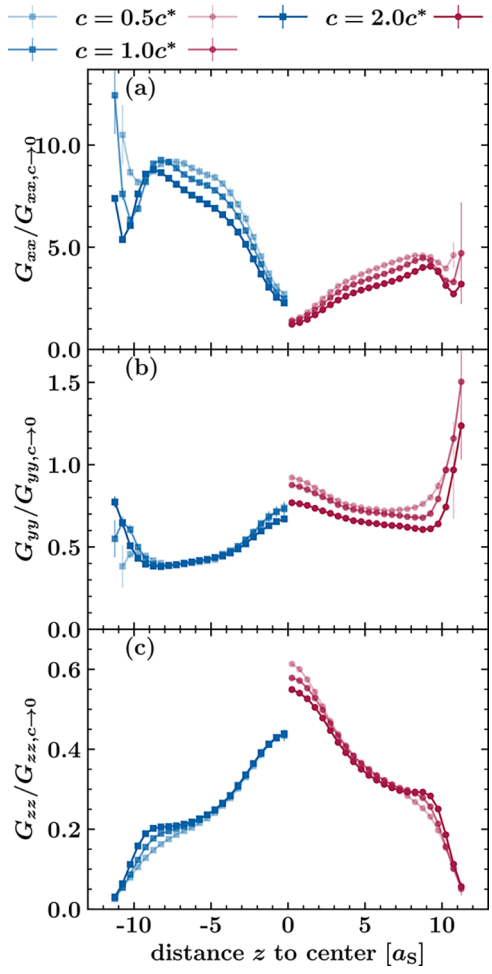

Figure 8. Diagonal components of the gyration tensor normalized by the ones in bulk at infinite dilution versus the distance to the channel center, for an average composition of N_L:N_R = 1:1 and 2 f_1 = 0.009 $m_S a_S t_0^{-1}$. (a) G_{xx} in flow direction, (b) G_{yy} in vorticity direction, and (c) G_{zz} in gradient direction. Chains are shown in blue squares and z < 0, rings in red circles and z > 0. With darkening hue, the concentration increases.

walls populating the channel center. Taking these effects together, the local ratio $\chi(z)$ of chains to rings is slightly higher than the average N_L:N_R in the center and lower close to the walls. When exposed to pressure-driven flow, this scenario reverses. In accordance with Figure 6, chains migrate toward the walls and deplete in the center, rings vice versa. Thus, the local ratio $\chi(z)$, shown as green lines in Figure 7, is lower than the average N_L:N_R in the center, when exposed to flow. Additionally, we find that cross-stream migration is enhanced with increasing flow strength. Interestingly, the spatial separation along the channel cross section of chains and rings persists for any investigated number ratio of chains and rings N_L:N_R. Therefore, this phenomenon can be used to separate chains and rings continuously by collecting the ring-enriched solution in the channel center and repeating the process. In doing so, the ring content will be constantly increased, representing an easy-to-build, high-throughput method to separate distinct polymeric topologies.

The increase in ring polymer content in the channel center is more pronounced at a higher flow strength for a fixed concentration, which can be correlated with higher Weissenberg numbers *Wi*. Furthermore, when the flow strength is constant, cross-stream migration of rings is stronger at higher concentrations, which correlates with lower Reynolds numbers *Re* and thus higher elasticity numbers *El*.

As soon as the Weissenberg number *Wi* exceeds unity, i.e., the inverse shear rate is larger than the longest relaxation time of a polymer, the polymer starts to deform. Since the shear rate varies across the channel cross section, being zero in the channel center and maximum close to the walls, we observe a deformation of the polymers dependent on the distance to the center, as shown in Figure 8a–c. Chains and rings start to elongate in the flow direction, as shown in Figure 8a, and to shrink in the vorticity and gradient direction, as shown in Figure 8b,c. The deformation is smallest in the channel center, where the shear gradient becomes zero. In addition, linear chains stretch more than rings in the flow direction, while they shrink stronger in the gradient direction since the chains relax slower. Further, rings are swollen compared to chains in the vorticity direction (see Figure 8b), an effect that has been observed previously.[15,67] It originates from solvent particles, which are reflected at the closed contour of ring polymers, resulting in a backflow that expands ring polymers in the vorticity direction. Since this swelling is caused by the rings' topology, it is absent for chains. Additionally, we see that this effect gets weaker with increasing concentration, due to the stronger screening of HI.

Both types of polymers show a concentration dependence when looking at the elongation in flow direction, as depicted in Figure 8a. When increasing the concentration, chains and rings are less deformed, which can be explained by the fact that the effective shear gradient decreases with increasing concentration, since u_{max} decreases. At the same time, the relaxation time of polymers increases with concentration, mitigating this

DOI: 10.1021/acs.macromol.9b01629
Macromolecules 2019, 52, 7858–7869

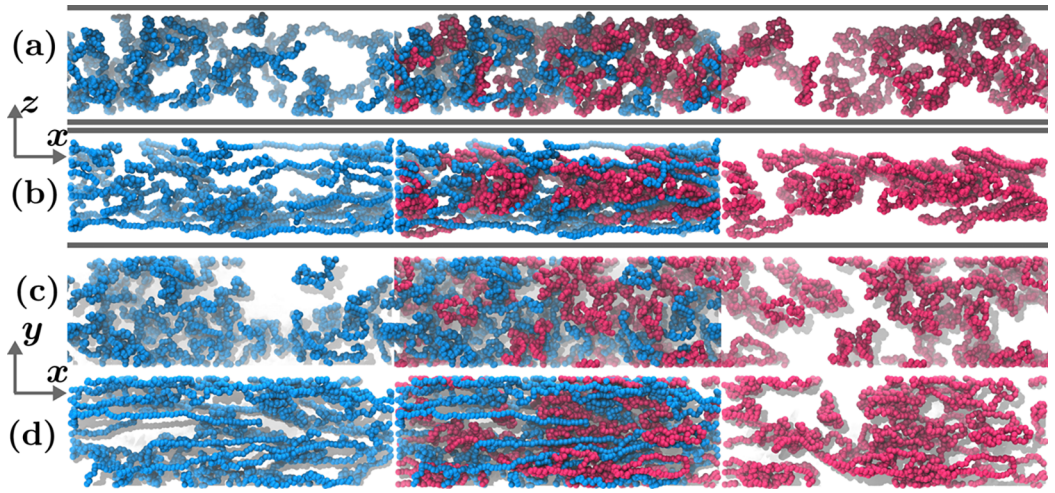

Figure 9. Simulation snapshots in the flow gradient (xz) plane at position $y = 0$ (a) at rest and (b) in flow; walls are indicated by the gray lines. Simulation snapshots in the flow vorticity (xy) plane at position $z = -L_z$ (c) at rest and (d) in flow; walls are omitted. *All* snapshots are for an average composition of N_L:N_R = 1:1 and $c = 0.5c^*$. To highlight differences, the middle column shows chains and rings, and the same picture is shown in the left and right columns omitting rings and chains, respectively. Chains are shown in blue, and rings in red.

effect. When calculating the Weissenberg number, both effects are taken into account, but since the relaxation time of polymers is derived from equilibrium, it does not take into account the reduced viscosity at higher shear rates due to shear thinning. Hence, the relaxation time of polymers is overestimated in the calculation of the Weissenberg number, leading to the apparent contradiction that polymers are less deformed at higher *Wi*. Moreover, we note that the shrinking of chains in the vorticity direction is unaffected by concentration, as shown in Figure 8b, and the shrinking of chains and rings in the gradient direction is unaffected as well, as depicted in Figure 8c. On the one hand, we expect that the polymers shrink with increasing concentration due to steric crowding. On the other hand, the maximum flow velocity (and hence the effective shear rate) decreases with increasing concentration, resulting in a less pronounced stretching. Here, we observe that these two effects cancel.

Since we find that the separation efficiency correlates with Weissenberg number *Wi* and inertia is non-negligible, one could explain the cross-stream migration and accumulation of rings in the channel center by elastic-inertial focusing, as shown experimentally[25,26] and in simulations.[27] The elastic force is based on gradients in normal stresses over the size of the tracer particle.[23] The higher the shear gradient, the higher the shear stress experienced by the polymers, which can be seen microscopically by a stronger elongation of polymers in flow direction (compare Figure 8a). The position-dependent deformation can be related to position-dependent normal stress differences $N_1 = \sigma_{xx} - \sigma_{zz}$ and $N_2 = \sigma_{zz} - \sigma_{yy}$,[68] leading to the focusing of tracer particles toward the center. In our setup, both rings and chains exert elastic forces. Since the relaxation time of chains is longer than the one of rings, its elastic force is stronger as well for a given shear rate. Note that here the elastic agent is not added to the solution, but intrinsically present owing to the differences in relaxation times of the two topologies.

In addition to the elastic force, inertia is non-negligible in our simulations, characterized by $Re > 1$. When applying the same flow strength to solutions of distinct concentrations, the increase in kinematic viscosity with increasing concentration is responsible for a decreasing Reynolds number, which correlates with an enhanced focusing as well as higher *El*. When increasing the flow strength, we have two competing effects: Qualitatively, we expect that the gradient of the first normal stress difference will increase with increasing flow velocity, as linear polymers are more extended. At the same time, the focused particles (rings) will shrink in gradient direction due to their extension in flow direction. It has been shown that the deformability of the focused particle influences its cross-stream migration in elastic-inertial flows.[32] Additionally, in shear thinning solutions, the Reynolds number is not anymore directly proportional to the maximum flow velocity, but influenced by the change in kinematic viscosity, which itself is a function of the effective shear rate. Thus, increasing the flow velocity in shear thinning solutions increases the Reynolds number with u_{max}^{2-n}, with n being the flow behavior index.

Inertia enables particles to cross streamlines, leading in the absence of elastic forces to shear-induced migration away from the center, as well as a wall-induced lift force toward the center, stabilizing an off-center position. Consistent with Figure 8b rings swell in the vorticity direction in flow, as can be seen also in the simulation snapshots shown in Figure 9d. The backflow responsible for the extension of ring polymers in the vorticity direction also enhances the repulsion from the walls. Due to this backflow, it is unfavorable for rings to extend close to the channel walls since the former will push them away. Additionally, we deduce from Figure 9d that, in flow, theoretically, the only possibility for rings to allocate close to the walls in a sea of extend chains is to form a two-folded ribbon, a conformation which is prevented by the aforementioned backflow and thus not observed. In contrast, in equilibrium, chains and rings form coils close to the walls, as shown in Figure 9c. The snapshots depicted in Figure 9a,b show additionally migration of rings from the walls (a) in a fluid at rest toward the center (b) when exposed to pressure-driven flow.

DOI: 10.1021/acs.macromol.9b01629
Macromolecules 2019, 52, 7858−7869

6. IMPACT OF HYDRODYNAMICS ON CROSS-STREAM MIGRATION AND POLYMER DEFORMATION

In equilibrium, the effect of HI becomes apparent when investigating dynamic quantities. Under flow, HI manifest themselves in (i) an additional lift force acting between the solute and the wall, which increases with increasing flow strength, apparent by comparing Figure 6a,c; (ii) the impact of solute on the flow profile, observable in Figure 3; and (iii) the momentum transfer between monomers, which exemplary can come into play as backflow, compare Section 5.

To investigate the effect of HI in more detail, we performed additional Langevin dynamics simulations that neglect hydrodynamics (see Section 2 for details) using HOOMD-blue version v2.2.5.[69,70] When coarse-graining the solvent further to a Langevin description, we need to decide which time scale should be conserved. As we hypothesize that the cross-stream migration is linked to the shear-induced polymer deformation, we decided to preserve the longest relaxation time. In equilibrium, the solvent velocity profile $\mathbf{v}_S$ noted in eq 8 is set to zero and we choose the friction coefficients ζ in the Langevin simulations to reproduce the diffusion of a single chain and a single ring at infinite dilution, respectively. Through adequately chosen friction coefficients ζ_L and ζ_R for chains and rings, we ensured that the deviation in the diffusion coefficient from our Langevin and MPC simulations is <5%. To verify whether this agreement holds true at higher concentration, we reproduced Figure 2 in the absence of hydrodynamics.

After having established a suitable mapping of MPC (HI) to Langevin dynamics (no HI) simulations in equilibrium, we performed Langevin simulations in flow, where we imposed the unperturbed, parabolic velocity flow profile of a pure solvent, as depicted in Figure 3. Figure 10a,b shows the number ratio $\chi(z)$ of chains to rings as a function of the distance to the channel center for $c = 0.5c^*$ and $c = 2c^*$, exemplary for an initial composition of N_L:N_R = 1:1 indicated by the gray dotted line. MPC simulations are shown in yellow (rest) and green (flow), whereas simulations without HI are shown in gray. In equilibrium, there is no impact of HI, as expected, resulting in perfect agreement between MPC and Langevin dynamics simulations. When applying a flow, rings accumulate in the center, lowering the ratio $\chi(z)$ below the average composition. In particular for low concentrations, compare Figure 10a, the cross-stream migration is more pronounced in the presence of HI. With increasing concentration, compare Figure 10b, those differences are less pronounced. Generally, HI are more important at lower concentration and vanish in the melt. Thus, HI enhance migration, most likely caused by an increased ring-wall lift force due to the stronger backflow created by the ring topology. Nevertheless, cross-stream migration persists even in a concentration regime $c > c^*$, where HI are less important, as can be deduced by more similar MPC and Langevin simulation results shown in Figure 10b. Thus, we hypothesize that the underlying mechanism can be explained by elastic-inertial focusing. Since this effect is related to a gradient in the first normal stress difference over the extension of the focused species, the elastic focusing force is conserved approximately by mapping the longest relaxation time scale of each topology when switching from MPC to Langevin simulation. Additional insights can be gained by carrying out simulations in the presence of hydrodynamics with rings and chains whose sizes are chosen in such a way that their relaxation times (at infinite dilution) are matched. This task is beyond the scope of the current manuscript, but we plan to systematically study the effects of polymer length and stiffness in work to follow.

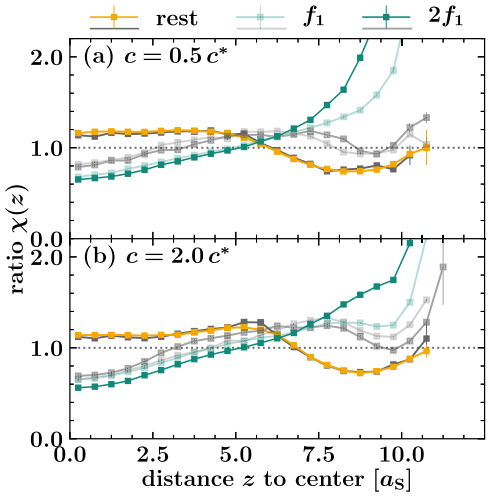

Figure 10. Number ratio χ as a function of the distance to the channel center for an average composition of N_L:N_R = 1:1 shown by the gray dotted line. MPC simulations are shown in yellow (rest) and green (flow), and Langevin simulations are shown in gray. With darkening color, the flow strength increases.

7. CONCLUSIONS

We investigated mixtures of linear and ring polymers at various concentrations and compositions, in bulk and when confined to a slit channel. We studied the systems at rest and under shear or pressure-driven flow. Hydrodynamic interactions were taken into account through the multiparticle collision algorithm coupled to molecular dynamics. To investigate the impact of hydrodynamics, we performed additional Langevin dynamics simulation without hydrodynamics. In equilibrium, we find that rings and chains shrink with increasing polymer concentration. Consistent with previous studies, rings shrink more compared to their linear counterpart. Since the investigated solutions are below the entanglement concentration, we do not see any impact of composition on diffusivities but find that it is purely a function of the monomer concentration c_M. Using shear simulations, we observe that the viscosity increases as well with monomer concentration. Hence, the topology-independent decrease in diffusivity is due to an increase in viscosity. Furthermore, we established that a single simulation of a polymer solution exposed to pressure-driven flow can replace several shear simulations of the same solution, when fitted with a power-law fluid model. We hypothesize that this approach can be used for any complex fluid replacing several shear simulations of distinct shear rates by a single simulation in pressure-driven flow, which covers intrinsically a continuum of shear rates. For a successful implementation, three prerequisites should be met: (i) a channel width being at least 2 times larger than the diameter of the solute, (ii) restricting the power-law-fluid fit to regions, which are accessible to the solute, and (iii) a cross-stream diffusion of solutes, which is slower than their relaxation.

When confining rings and chains to a slit channel at rest, we find that rings show a stronger tendency to accumulate close to

DOI: 10.1021/acs.macromol.9b01629
Macromolecules 2019, 52, 7858−7869

the walls compared to chains for all investigated compositions. When applying a pressure-driven flow, this behavior changes drastically in mixtures of chains and rings. Here, rings accumulate in the channel center and chains migrate toward the walls. In contrast, chains accumulate in the center of the channel in the absence of rings. We find that cross-stream migration persists for all compositions, being more pronounced with increasing polymer concentration and flow strength.

These results open novel routes toward the separation of mixtures of linear and ring polymers. Since ring polymers accumulate in the channel center in ring-chain mixtures exposed to pressure-driven flow, spatially collecting the center fraction results in a solution with increased ring content. Repeating the process iteratively allows to purify mixtures of any initial stoichiometry at high mass throughput.

■ ASSOCIATED CONTENT

Supporting Information

The Supporting Information is available free of charge on the ACS Publications website at DOI: 10.1021/acs.macromol.9b01629.

Start configurations of polymers provided for reproducibility (ZIP)

An explanatory document (PDF)

■ AUTHOR INFORMATION

Corresponding Authors

*E-mail: lisa.weiss@univie.ac.at (L.B.W.).

*E-mail: christos.likos@univie.ac.at (C.N.L.).

*E-mail: anikouba@uni-mainz.de (A.N.).

ORCID

Lisa B. Weiss: 0000-0003-4255-6712

Christos N. Likos: 0000-0003-3550-4834

Arash Nikoubashman: 0000-0003-0563-825X

Notes

The authors declare no competing financial interest.

■ ACKNOWLEDGMENTS

This project received funding from the European Union's Horizon 2020 Research and Innovation Programme under Grant Agreement No. 674979-NANOTRANS. A.N. acknowledges funding from the German Research Foundation (DFG) under Project No. NI 1487/2-1.

■ REFERENCES

(1) Campbell, N. A.; Reece, J. B.; Urry, L. A.; Cain, M. L.; Wasserman, S. A.; Minorsky, P. V.; Jackson, R. B. *Campbell Biology*, 10th ed.; Pearson: Boston, 2013.

(2) Wasserman, S. A.; Cozzarelli, N. R. Biochemical Topology: Applications to DNA Recombination and Replication. *Science* **1986**, *232*, 951−960.

(3) Arsuaga, J.; Vazquez, M.; Trigueros, S.; Sumners, D. W.; Roca, J. Knotting probability of DNA molecules confined in restricted volumes: DNA knotting in phage capsids. *Proc. Natl. Acad. Sci. USA* **2002**, *99*, 5373−5377.

(4) Arsuaga, J.; Vazquez, M.; McGuirk, P.; Trigueros, S.; Sumners, D. W.; Roca, J. DNA knots reveal a chiral organization of DNA in phage capsids. *Proc. Natl. Acad. Sci. USA* **2005**, *102*, 9165−9169.

(5) Lasda, E.; Parker, R. Circular RNAs: diversity of form and function. *RNA* **2014**, *20*, 1829−1842.

(6) Jeck, W. R.; Sharpless, N. E. Detecting and characterizing circular RNAs. *Nat. Biotechnol.* **2014**, *32*, 453−461.

(7) McLeish, T. Polymers Without Beginning or End. *Science* **2002**, *297*, 2005.

(8) Kaitz, J. A.; Diesendruck, C. E.; Moore, J. S. End group characterization of poly(phthalaldehyde): Surprising discovery of a reversible, cationic macrocyclization mechanism. *J. Am. Chem. Soc.* **2013**, *135*, 12755−12761.

(9) Robertson, R. M.; Laib, S.; Smith, D. E. Diffusion of isolated DNA molecules: Dependence on length and topology. *Proc. Natl. Acad. Sci. USA* **2006**, *103*, 7310−7314.

(10) Narros, A.; Likos, C. N.; Moreno, A. J.; Capone, B. Multi-blob coarse graining for ring polymer solutions. *Soft Matter* **2014**, *10*, 9601−9614.

(11) Zhou, Y.; Hsiao, K.-W.; Regan, K. E.; Kong, D.; McKenna, G. B.; Robertson-Anderson, R. M.; Schroeder, C. M. Effect of molecular architecture on ring polymer dynamics in semidilute linear polymer solutions. *Nat. Commun.* **2019**, *10*, 1753.

(12) Robertson, R. M.; Smith, D. E. Self-diffusion of entangled linear and circular DNA molecules: Dependence on length and concentration. *Macromolecules* **2007**, *40*, 3373−3377.

(13) Robertson, R. M.; Smith, D. E. Strong effects of molecular topology on diffusion of entangled DNA molecules. *Proc. Natl. Acad. Sci. USA* **2007**, *104*, 4824−4827.

(14) Chapman, C. D.; Shanbhag, S.; Smith, D. E.; Robertson-Anderson, R. M. Complex effects of molecular topology on diffusion in entangled biopolymer blends. *Soft Matter* **2012**, *8*, 9177−9182.

(15) Hsiao, K.-W.; Schroeder, C. M.; Sing, C. E. Ring Polymer Dynamics Are Governed by a Coupling between Architecture and Hydrodynamic Interactions. *Macromolecules* **2016**, *49*, 1961−1971.

(16) Li, Y.; Hsiao, K.-W.; Brockman, C. A.; Yates, D. Y.; Robertson-Anderson, R. M.; Kornfield, J.; San Francisco, M. J.; Schroeder, C. M.; McKenna, G. B. When Ends Meet: Circular DNA Stretches Differently in Elongational Flows. *Macromolecules* **2015**, *48*, 5997−6001.

(17) Kapnistos, M.; Lang, M.; Vlassopoulos, D.; Pyckhout-Hintzen, W.; Richter, D.; Cho, D.; Chang, T.; Rubinstein, M. Unexpected power-law stress relaxation of entangled ring polymers. *Nat. Mater.* **2008**, *7*, 997−1002.

(18) Segré, G.; Silberberg, A. Radial Particle Displacement in Poiseuille Flow of Suspensions. *Nature* **1961**, *189*, 209−210.

(19) Di Carlo, D.; Irimia, D.; Tompkins, R. G.; Toner, M. Continuous inertial focusing, ordering, and separation of particles in microchannels. *Proc. Natl. Acad. Sci. USA* **2007**, *104*, 18892−18897.

(20) Zhou, J.; Papautsky, I. Fundamentals of inertial focusing in microchannels. *Lab Chip* **2013**, *13*, 1121−1132.

(21) Asmolov, E. S. The inertial lift on a spherical particle in a plane Poiseuille flow at large channel Reynolds number. *J. Fluid Mech.* **1999**, *381*, 63−87.

(22) Ma, H.; Graham, M. D. Theory of shear-induced migration in dilute polymer solutions near solid boundaries. *Phys. Fluids* **2005**, *17*, No. 083103.

(23) Leshansky, A. M.; Bransky, A.; Korin, N.; Dinnar, U. Tunable nonlinear viscoelastic "focusing" in a microfluidic device. *Phys. Rev. Lett.* **2007**, *98*, No. 234501.

(24) Del Giudice, F.; Romeo, G.; D'Avino, G.; Greco, F.; Netti, P. A.; Maffettone, P. L. Particle alignment in a viscoelastic liquid flowing in a square-shaped microchannel. *Lab Chip* **2013**, *13*, 4263−4271.

(25) Yang, S.; Kim, J. Y.; Lee, S. J.; Lee, S. S.; Kim, J. M. Sheathless elasto-inertial particle focusing and continuous separation in a straight rectangular microchannel. *Lab Chip* **2011**, *11*, 266−273.

(26) Kang, K.; Lee, S. S.; Hyun, K.; Lee, S. J.; Kim, J. M. DNA-based highly tunable particle focuser. *Nat. Commun.* **2013**, *4*, No. 2567.

(27) Howard, M. P.; Panagiotopoulos, A. Z.; Nikoubashman, A. Inertial and viscoelastic forces on rigid colloids in microfluidic channels. *J. Chem. Phys.* **2015**, *142*, No. 224908.

(28) Lim, E. J.; Ober, T. J.; Edd, J. F.; Desai, S. P.; Neal, D.; Bong, K. W.; Doyle, P. S.; McKinley, G. H.; Toner, M. Inertio-elastic focusing of bioparticles in microchannels at high throughput. *Nat. Commun.* **2014**, *5*, No. 4120.

DOI: 10.1021/acs.macromol.9b01629
Macromolecules 2019, 52, 7858−7869

(29) D'Avino, G.; Romeo, G.; Villone, M. M.; Greco, F.; Netti, P.; Maffettone, P. L. Single line particle focusing induced by viscoelasticity of the suspending liquid: theory, experiments and simulations to design a micropipe flow-focuser. *Lab Chip* **2012**, *12*, 1638−1645.
(30) Go, T.; Byeon, H.; Lee, S. J. Focusing and alignment of erythrocytes in a viscoelastic medium. *Sci. Rep.* **2017**, *7*, No. 41162.
(31) Yang, S.; Lee, S. S.; Ahn, S. W.; Kang, K.; Shim, W.; Lee, G.; Hyun, K.; Kim, J. M. Deformability-selective particle entrainment and separation in a rectangular microchannel using medium viscoelasticity. *Soft Matter* **2012**, *8*, 5011−5019.
(32) Howard, M. P.; Truskett, T. M.; Nikoubashman, A. Cross-stream migration of a Brownian droplet in a polymer solution under Poiseuille flow. *Soft Matter* **2019**, *15*, 3168−3178.
(33) Weiss, L. B.; Nikoubashman, A.; Likos, C. N. Topology-Sensitive Microfluidic Filter for Polymers of Varying Stiffness. *ACS Macro Lett.* **2017**, *6*, 1426−1431.
(34) Weeks, J. D.; Chandler, D.; Andersen, H. C. Role of Repulsive Forces in Determining the Equilibrium Structure of Simple Liquids. *J. Chem. Phys.* **1971**, *54*, 5237−5247.
(35) Rubinstein, M.; Colby, R. H. *Polymer Physics*; Oxford University Press: Oxford, 2003.
(36) Bishop, M.; Kalos, M. H.; Frisch, H. L. Molecular dynamics of polymeric systems. *J. Chem. Phys.* **1979**, *70*, 1299−1304.
(37) Kremer, K.; Grest, G. S. Dynamics of entangled linear polymer melts: A molecular dynamics simulation. *J. Chem. Phys.* **1990**, *92*, 5057−5086.
(38) Malevanets, A.; Kapral, R. Continuous-velocity lattice-gas model for fluid flow. *Europhys. Lett.* **1998**, *44*, 552−558.
(39) Malevanets, A.; Kapral, R. Mesoscopic model for solvent dynamics. *J. Chem. Phys.* **1999**, *110*, 8605−8613.
(40) Howard, M. P.; Nikoubashman, A.; Palmer, J. C. Modeling hydrodynamic interactions in soft materials with multiparticle collision dynamics. *Curr. Opin. Chem. Eng.* **2019**, *23*, 34−43.
(41) Jendrejack, R. M.; Schwartz, D. C.; De Pablo, J. J.; Graham, M. D. Shear-induced migration in flowing polymer solutions: Simulation of long-chain DNA in microchannels. *J. Chem. Phys.* **2004**, *120*, 2513−2529.
(42) Usta, O. B.; Ladd, A. J. C.; Butler, J. E. Lattice-Boltzmann simulations of the dynamics of polymer solutions in periodic and confined geometries. *J. Chem. Phys.* **2005**, *122*, No. 094902.
(43) Cannavacciuolo, L.; Winkler, R. G.; Gompper, G. Mesoscale simulations of polymer dynamics in microchannel flows. *Europhys. Lett.* **2008**, *83*, No. 34007.
(44) Zimm, B. H. Dynamics of Polymer Molecules in Dilute Solution: Viscoelasticity, Flow Birefringence and Dielectric Loss. *J. Chem. Phys.* **1956**, *24*, 269−278.
(45) Mussawisade, K.; Ripoll, M.; Winkler, R. G.; Gompper, G. Dynamics of polymers in a particle-based mesoscopic solvent. *J. Chem. Phys.* **2005**, *123*, No. 144905.
(46) Rouse, P. E. A Theory of the Linear Viscoelastic Properties of Dilute Solutions of Coiling Polymers. *J. Chem. Phys.* **1953**, *21*, 1272−1280.
(47) Dahirel, V.; Zhao, X.; Couet, B.; Batôt, G.; Jardat, M. Hydrodynamic interactions between solutes in multiparticle collision dynamics. *Phys. Rev. E* **2018**, *98*, No. 053301.
(48) Ihle, T.; Kroll, D. M. Stochastic rotation dynamics: A Galilean-invariant mesoscopic model for fluid flow. *Phys. Rev. E* **2001**, *63*, No. 020201.
(49) Ihle, T.; Kroll, D. M. Stochastic rotation dynamics. I. Formalism, Galilean invariance, and Green-Kubo relations. *Phys. Rev. E* **2003**, *67*, No. 066705.
(50) Kikuchi, N.; Pooley, C. M.; Ryder, J. F.; Yeomans, J. M. Transport coefficients of a mesoscopic fluid dynamics model. *J. Chem. Phys.* **2003**, *119*, 6388−6395.
(51) Tüzel, E.; Strauss, M.; Ihle, T.; Kroll, D. M. Transport coefficients for stochastic rotation dynamics in three dimensions. *Phys. Rev. E* **2003**, *68*, No. 036701.
(52) Ripoll, M.; Mussawisade, K.; Winkler, R.; Gompper, G. Dynamic regimes of fluids simulated by multiparticle-collision dynamics. *Phys. Rev. E* **2005**, *72*, No. 016701.
(53) Lamura, A.; Gompper, G.; Ihle, T.; Kroll, D. M. Multi-particle collision dynamics: Flow around a circular and a square cylinder. *Europhys. Lett.* **2001**, *56*, 319−325.
(54) Götze, I. O.; Noguchi, H.; Gompper, G. Relevance of angular momentum conservation in mesoscale hydrodynamics simulations. *Phys. Rev. E* **2007**, *76*, No. 046705.
(55) Huang, C. C.; Chatterji, A.; Sutmann, G.; Gompper, G.; Winkler, R. G. Cell-level canonical sampling by velocity scaling for multiparticle collision dynamics simulations. *J. Comput. Phys.* **2010**, *229*, 168−177.
(56) Müller-Plathe, F. Reversing the perturbation in nonequilibrium molecular dynamics: An easy way to calculate the shear viscosity of fluids. *Phys. Rev. E* **1999**, *59*, 4894−4898.
(57) Petersen, M. K.; Lechman, J. B.; Plimpton, S. J.; Grest, G. S.; in't Veld, P. J.; Schunk, P. R. Mesoscale hydrodynamics via stochastic rotation dynamics: Comparison with Lennard-Jones fluid. *J. Chem. Phys.* **2010**, *132*, No. 174106.
(58) Statt, A.; Howard, M. P.; Panagiotopoulos, A. Z. Unexpected secondary flows in reverse nonequilibrium shear flow simulations. *Phys. Rev. Fluids* **2019**, *4*, No. 043905.
(59) Yeh, I. C.; Hummer, G. System-size dependence of diffusion coefficients and viscosities from molecular dynamics simulations with periodic boundary conditions. *J. Phys. Chem. B* **2004**, *108*, 15873−15879.
(60) Huang, C. C.; Winkler, R. G.; Sutmann, G.; Gompper, G. Semidilute polymer solutions at equilibrium and under shear flow. *Macromolecules* **2010**, *43*, 10107−10116.
(61) Daoud, M.; Cotton, J. P.; Farnoux, B.; Jannink, G.; Sarma, G.; Benoit, H.; Duplessix, C.; Picot, C.; de Gennes, P. G. Solutions of Flexible Polymers. Neutron Experiments and Interpretation. *Macromolecules* **1975**, *8*, 804−818.
(62) Sakaue, T. Ring polymers in melts and solutions: Scaling and crossover. *Phys. Rev. Lett.* **2011**, *106*, No. 167802.
(63) Batôt, G.; Dahirel, V.; Mériguet, G.; Louis, A. A.; Jardat, M. Dynamics of solutes with hydrodynamic interactions: Comparison between Brownian dynamics and stochastic rotation dynamics simulations. *Phys. Rev. E* **2013**, *88*, No. 043304.
(64) Schroeder, C. M.; Teixeira, R. E.; Shaqfeh, E. S. G.; Chu, S. Dynamics of DNA in the Flow-Gradient Plane of Steady Shear Flow: Observations and Simulations. *Macromolecules* **2005**, *38*, 1967−1978.
(65) Pan, S.; Nguyen, D. A.; Dünweg, B.; Sunthar, P.; Sridhar, T.; Ravi Prakash, J. Shear thinning in dilute and semidilute solutions of polystyrene and DNA. *J. Rheol.* **2018**, *62*, 845−867.
(66) Chubak, I.; Locatelli, E.; Likos, C. N. Ring polymers are much stronger depleting agents than linear ones. *Mol. Phys.* **2018**, *116*, 2911−2926.
(67) Liebetreu, M.; Ripoll, M.; Likos, C. N. Trefoil Knot Hydrodynamic Delocalization on Sheared Ring Polymers. *ACS Macro Lett.* **2018**, *7*, 447−452.
(68) Doi, M., Edwards, S. *The Theory of Polymer Dynamics*; Clarendon Press: Oxford, 1986.
(69) Anderson, J. A.; Lorenz, C. D.; Travesset, A. General purpose molecular dynamics simulations fully implemented on graphics processing units. *J. Comput. Phys.* **2008**, *227*, 5342−5359.
(70) Glaser, J.; Nguyen, T. D.; Anderson, J. A.; Lui, P.; Spiga, F.; Millan, J. A.; Morse, D. C.; Glotzer, S. C. Strong scaling of general-purpose molecular dynamics simulations on GPUs. *Comput. Phys. Commun.* **2015**, *192*, 97−107.

DOI: 10.1021/acs.macromol.9b01629
Macromolecules 2019, 52, 7858−7869